Three-Component Force Measurements on a Large Scramjet in a Shock Tunnel

M. J. Robinson[*] and D. J. Mee[†]
University of Queensland, Brisbane, Queensland 4072, Australia
and
C. Y. Tsai[‡] and R. J. Bakos[§]
Allied Aerospace Industries, Ronkonkoma, New York 11779

A stress-wave force balance for measurement of thrust, lift, and pitching moment on a large scramjet model (40 kg in mass, 1.165 m in length) in a reflected shock tunnel has been designed, calibrated, and tested. Transient finite element analysis was used to model the performance of the balance. This modeling indicates that good decoupling of signals and low sensitivity of the balance to the distribution of the load can be achieved with a three-bar balance. The balance was constructed and calibrated by applying a series of point loads to the model. A good comparison between finite element analysis and experimental results was obtained with finite element analysis aiding in the interpretation of some experimental results. Force measurements were made in a shock tunnel both with and without fuel injection, and measurements were compared with predictions using simple models of the scramjet and combustion. Results indicate that the balance is capable of resolving lift, thrust, and pitching moments with and without combustion. However vibrations associated with tunnel operation interfered with the signals indicating the importance of vibration isolation for accurate measurements.

Nomenclature

A	=	axial force, N
C_L	=	lift coefficient, $2L/\rho v^2 S$
C_M	=	moment coefficient, $2M/\rho v^2 SD$
C_T	=	thrust coefficient, $2T/\rho v^2 S$
D	=	reference length, 1.0 m
F	=	scaling factor
G	=	impulse response matrix
g	=	impulse response vector
L	=	lift force, N
M	=	pitching moment (about balance center), N · m
Ma	=	Mach number
$\dot{m}$	=	mass flow rate, kg/m^3
N	=	normal force, N
p	=	pressure, Pa
Q	=	temperature, K
Re	=	Reynolds number
S	=	reference area, m^2
T	=	thrust force, N
t	=	time, s
u	=	input vector
v	=	velocity, m/s
y	=	output vector
$\epsilon_a(t)$	=	strain in aft bar
$\epsilon_b(t)$	=	strain in axial bar
$\epsilon_f(t)$	=	strain in forward bar
ρ	=	density, kg/m^3
τ	=	shifted time, s
Φ	=	equivalence ratio

Subscripts

A	=	axial direction
M	=	moment direction
N	=	normal direction
P	=	pitot
s	=	nozzle supply conditions
θ	=	momentum thickness
∞	=	freestream condition

Introduction

INTEGRATED force and moment data are crucial for the successful development of aerodynamic and aeropropulsive systems. With engine integration into the airframe of hypersonic flight vehicles, such as in the HyperX scramjet experiment,[1] the operation of the engine has a significant influence on the aerodynamic performance of the entire vehicle. It would be advantageous in such cases to be able to make ground-test measurements of the aerodynamic performance of the vehicle with the engines operating. However when it comes to hypersonic vehicles, reproducing hypersonic flight conditions above Mach 8 on the ground is usually restricted to impulse tunnels with test times lasting only several milliseconds. These short test times preclude the use of conventional force-balance techniques for models of typical size.[2]

Because of the difficulties in measuring the aerodynamic performance of fueled scramjet-integrated vehicles, separate component tests are sometimes combined or integrated with theoretical analysis or computational-fluid-dynamics (CFD) calculations to determine the overall performance of a vehicle (e.g., Refs. 3 and 4). Most of the testing that has been done to directly measure forces associated with combusting scramjet engines has been restricted to direct-connect tests in facilities with longer duration flows, such as vitiated-air blowdown tunnels (e.g., Refs. 5 and 6).

Advances have been made in the past decade on techniques for measuring forces in flows with very short durations, such as occur in impulse hypersonic facilities (e.g., Refs. 7–9). One technique, which has been shown to be quite suitable for force measurement in impulse facilities, is the stress-wave force-balance technique, originally proposed for single-component (drag) force measurement.[10] This technique has been extended for measurement of the three components of force on a cone at incidence[11] and has been used to measure the thrust produced by scramjet vehicles, with fuel injection

and combustion, for models with symmetry about the thrust axis.[12,13] Takahashi et al.[14] used a series of accelerometers located on a scramjet model to infer the combined effects of aerodynamic and propulsive forces in a series of tests in the High Enthalpy Shock Tunnel (HIEST).

The purpose of the study reported in this paper was to investigate whether a three-component stress-wave force balance could be built for measurements of lift, thrust, and pitching moment on a large, fueled scramjet model (incorporating an inlet, combustion chamber, and a thrust surface). The basic principle of operation of a stress-wave force balance is to model the arrangement of the test model and the associated force-balance arrangement as a linear system. In its simplest (single-component) form a force-balance system has an input $u(t)$ (the aerodynamic load on the model), an output $y(t)$ (a response measured in the support structure for the model, typically a strain measurement), and an impulse response $g(t)$, which indicates the relationship between the input and output. The relationship among these parameters can then be expressed in terms of a convolution integral

$$y(t) = \int_0^t g(t-\tau)u(\tau)\,d\tau \tag{1}$$

If the impulse response is known (via an experimental calibration or finite element modelling) and the output time history is measured in an experiment, it is then possible to determine the time history of the aerodynamic force applied to the model using a numerical deconvolution procedure.

If the time signals for the input, output, and impulse response are discretized with uniform time step Δt, Eq. (1) becomes

$$y = Gu\Delta t \tag{2}$$

Here, u and y are vectors formed from the discretized input and output signals, and G is a square, lower-triangular, matrix formed from the discretized impulse response.

Consider a balance for measurement of the three force components in one plane. Let the forces in orthogonal directions be designated normal N and axial A, and let the couple in that plane be designated moment M. Consider a case where there are three independent output signals that are measured. Ideally, each of the three signals responds primarily to one of the input loads. If the signals are discretized at time step Δt, the three output vectors y_N, y_A, and y_M can be related to the three input signals u_N, u_A, and u_M, via

$$\begin{pmatrix} y_N \\ y_A \\ y_M \end{pmatrix} = \begin{bmatrix} G_{NN} & G_{NA} & G_{NM} \\ G_{AN} & G_{AA} & G_{AM} \\ G_{MN} & G_{MA} & G_{MM} \end{bmatrix} \begin{pmatrix} u_N \\ u_A \\ u_M \end{pmatrix} \Delta t \tag{3}$$

In this case there are nine square submatrices relating each of the outputs to each of the inputs. As with conventional force balances, it is preferable to minimize the coupling terms (the off-diagonal submatrices in this case), but it is usually not possible to eliminate them completely.

As for the single-component balance, the impulse responses are found either experimentally or using finite element modeling. In an experiment in a wind tunnel, the time histories of the applied loads are determined from the three measured output signals using multiple-component deconvolution techniques based on the algorithm proposed by Prost and Goutte.[15] The algorithm solves the discrete convolution equation using functional minimization with the extended conjugate gradient algorithm.

This paper presents results obtained for a thrust, lift, and pitching-moment balance applied to a large scramjet model. Details of the scramjet model and force balance are given. Results from dynamic finite element simulations of the force balance illustrating the sensitivity to loading distribution are considered in the paper. The experimental calibration of the force balance and comparison with the finite element simulations are presented, and estimation of the experimental forces acting on the scramjet model are shown. Lastly, results obtained in the HYPULSE reflected shock tunnel at GASL, Inc., are presented.

Scramjet Model and Force Balance

The scramjet model (Figs. 1 and 2) was originally designed and constructed by GASL, Inc., for tests that were performed in the PGU facility at the Central Research Institute for Machine Building (TSNIIMASH) in the mid-1990s.[16] The scramjet has a spatular inlet that is 300 mm long and has a sharp leading edge with an included angle of 16.5 deg. The inlet is 281 mm wide at its leading edge and tapers to a width of 125 mm at entrance to the combustor. The combustion chamber is 100 mm wide and is enclosed by a cowl to give a chamber height of 51 mm. The cross-sectional area of the combustor remains constant over its length of 500 mm. A line of 15 fuel injection ports spanning the width of the combustion chamber are located 95 mm aft of the combustor entrance. Each port consists of a 10-deg conical hole providing a fuel-injection Mach number
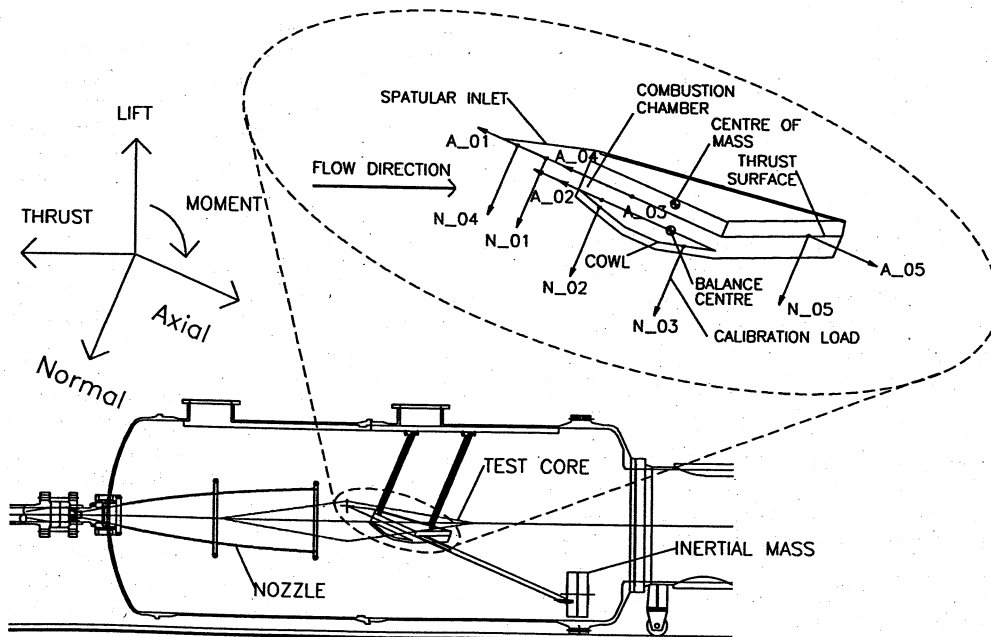

Fig. 1 NASA/GASL generic hypersonic combustor model positioned in the HYPULSE test section and load calibration points.
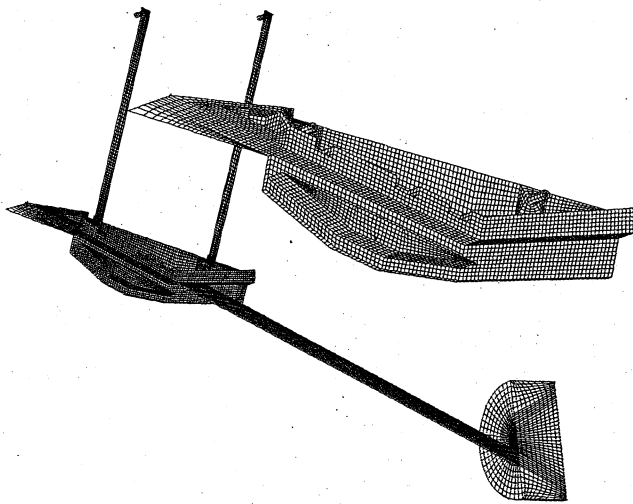
Fig. 2 Finite element mesh of force balance and NASA/GASL scramjet model.

of 2. The cowl has a sharp leading edge with an included angle of 15 deg. Beyond 188 mm from its leading edge, the cowl thickness is constant at 51 mm and remains so for 124 mm. It then decreases in thickness at an angle of 15 deg to give a sharp trailing edge at the end of the combustor. The thrust surface is 100 mm wide and 400 mm long and is inclined at an angle of 24 deg to the surface of the combustion chamber. The side plates of the scramjet are 12.5 mm thick and extend 26 mm beyond the external surface of the cowl and 71 mm beyond the thrust surface. The leading edges of the side plates are sharp with a bevel angle of 16 deg. The cavity downstream of the spatular inlet and above the combustor and thrust surface is covered with a 6.4-mm-thick flat plate (not shown in Fig. 2). The model, made primarily of aluminum, is in excess of 40 kg in mass and is 1.165 m in total length.

The model was positioned with the inlet at 23-deg angle of attack with bumper supports to protect against significant sideways movement. This angle of attack meant that the thrust surface was inclined at only -1 deg to the direction of flow upstream of the model. Thus, a pressure increase on this surface as a result of combustion can produce a substantial change in lift but not much change in thrust. The present scramjet was designed for combustion studies and was not intended to produce net thrust. Nevertheless it consists of an inlet, combustion chamber, and thrust surface and serves as a good test for the implementation of a stress-wave force balance on a complete scramjet vehicle with fuel combustion.

Previous multiple-component stress-wave force balances have been based on a model attached to a single long stress bar via a number of short connecting arms.[11,17] In the present design the scramjet model is supported by two, pin-jointed, parallel bars and one, longer, stress bar oriented perpendicular to these bars. The coordinate system to be used for the balance is aligned with the bars. The direction of the long stress bar is referred to as the axial direction and the direction of the two shorter bars as the normal direction (Fig. 1). The 2-m-long axial stress bar is made from a solid brass bar of 25×50 mm cross section and is rigidly attached at one end to the thrust surface of the model and at the other end to a large (300 kg) inertial mass, which rests on a rubber pad on the floor of the test section. The bar is oriented with the 50-mm dimension being in the vertical plane, and the first 400 mm of the brass bar, closest to the model, is fared to reduce interference with the flow. In retrospect, it would have been better to attach the axial bar at the base of the thrust surface to minimize interference with the flow. The two parallel normal bars are made of 25×25 mm steel bar and are pinned to the model and to the top of the dump tank. The forward normal bar is 0.94 m long, and the aft normal bar is 1.11 m long. Each of the normal stress bars was aerodynamically shielded by a section of angle iron rigidly attached to the top of the test section. The brass bar was also aerodynamically shielded, for all but the first 200 mm of the bar, by enclosing it in a rectangular section tube that was rigidly attached to the inertial mass

and supported from the floor of the test section. The inlet and most of the model were contained in the conical test core of the nozzle. However, as shown in Fig. 1, the rear of the cowl and the thrust surface extended beyond the downstream end of the nominal test core.

Semiconductor strain gauges, connected in a bending-compensation arrangement in a half Wheatstone bridge, and sections of 20-mm-wide piezoelectric film[18] were used to measure time histories of strain in the directions of the axes of the bars. The brass axial bar and the aft normal bar were instrumented with both types of gauges, but the forward normal bar had only a piezoelectric gauge.

The piezoelectric film gauges were used for processing the data from the shots in the tunnel because the semiconductor gauges were more sensitive to electrical noise during those tests. The signals from the two types of gauges could be compared in the calibration tests, and good agreement was observed for the signals from the gauges on the aft normal bar. The signals from the piezoelectric film gauge on the axial bar, which had a different amplifier from that on the aft normal bar, showed evidence of having a short time constant with the response to a step drifting back toward zero. The film gauge on the forward normal bar had the same type of amplifier as that on the axial bar, and there was evidence that this signal also drifted toward zero in response to a step. In both of the system identification tests (i.e., the dynamic calibration of the model) and the tunnel tests, the same measurement system was used, including the same amplifiers and data-acquisition system. Thus, the drift in the signals from the piezo-film gauges is included in the system impulse responses obtained from the calibrations and in the signals from the tunnel shots and is implicitly included in the processing of the results.

The three output signals [to be used with Eq. (3)] are

$$y_N(t) = \epsilon_f(t) + F\epsilon_a(t), \qquad y_A(t) = \epsilon_b(t)$$

$$y_M(t) = \epsilon_f(t) - F\epsilon_a(t) \tag{4}$$

The factor F is a scaling factor chosen to minimize coupling of the output signals. This results in the output signal y_N responding primarily to a pure normal force, the signal y_A responding primarily to a pure axial force, and the signal y_M responding primarily to a pure moment. The moments are taken about a point on the lower surface of the combustion chamber, which is midway between the two normal bars making the center of the balance 647 mm from the leading edge of the inlet.

Finite Element Simulations

Finite element analysis (FEA) has proven to be a useful tool in the design of stress-wave force balances.[17,19] Because the behavior of the balance is dynamic in nature, FEA is able to model the balance response and enables proposed balance designs to be investigated.

A detailed model (Fig. 2) was constructed to investigate the performance of the design under varying load conditions. The finite element model was developed using MSC-PATRAN (which served as a pre- and postprocessor) and was solved with MSC-NASTRAN using the direct linear transient solution.[20] These packages were run on a Silicon Graphics Challenge Array with a maximum throughput of 7.2 GigaFLOPS. The model incorporated symmetry along the central plane of the scramjet to reduce the computation time.

The nodes along the central axis of the large inertial mass were attached to grounded springs and dampers in order to model the rubber pad. The pin tips on the end of the normal bars were fixed in all directions. The model was composed of approximately 20,000 solid HEX8 and a small number of solid WEDGE6 elements. Structural damping was not employed. Other points such as integration time step, mesh refinement, and mesh transition factors were adapted from Daniel and Mee.[19]

Modeling of the pin joints was achieved by using linear multipoint constraints (MPCs), which allow movement of the pin nodes in the tangential direction but restrict movement radially. The MPCs were applied to the outer surface of each pin and to the inner surface of each housing. Modeling the pin joints with MPCs assumes that the motion of the pin is linear and remains in complete contact during

rotation. A more realistic approach would incorporate the use of contact surface elements; however, time-dependent contact details of the pin would be needed. Further, a nonlinear solution would be required, which adds greatly to computational resources. For these reasons linear MPCs were employed. Experimental results exploring the linearity of the balance give merit to this assumption. However, it should be emphasized that the purpose of using FEA in the design and analysis of stress-wave force balances is to give general trends as to the performance of the balance and is usually used as a design tool.

To determine the dynamic behavior of the balance, a total of 10 step point loads was applied (five normal forces, designated N_01-N_05, and five axial forces, designated A_01-A_05, as shown in Fig. 1). Dynamic FEA was performed, producing a total of 30 strain time histories (three for each load case). For each of the 10 load cases, the strain signals were monitored at locations on the FEA model that corresponded to locations of the strain gauges on the bars in the experiments. The strains were averaged over several elements to account for the lengths of the strain sensing elements used in the experiments. From these simulations the axial y_A, normal y_N, and moment y_M responses to each of the applied loads can be found using Eq. (4).

Typical strain output signals for each of the three bars are shown for a step application of a pure axial force at time zero in Fig. 3a. The
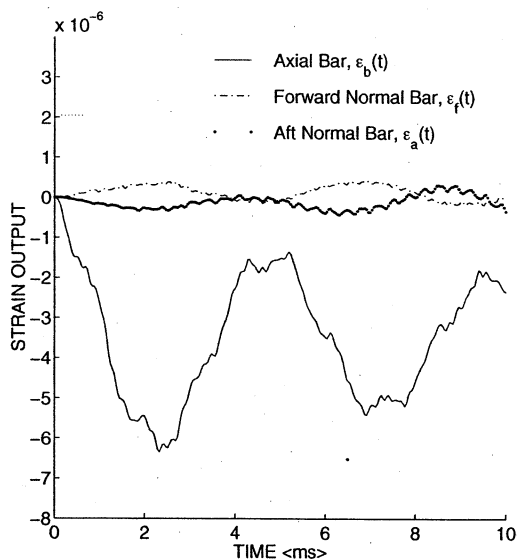
a) Stress bar responses for an axial load
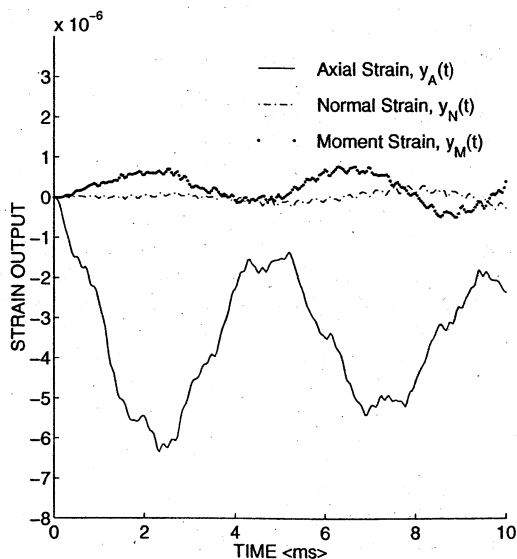
b) y_N, y_A, and y_M strain signals for an axial load

Fig. 3   Examples of FEA strain signals. Step responses for an axial load applied at location A_04.

three output signals for this case, calculated using Eq. (4), are shown in Fig. 3b. The fact that the y_N and y_M signals in Fig. 3b are nonzero shows that there is some coupling between the normal and moment signals and axial loading (a pure axial load was applied). However, the magnitude of the y_N and y_M signals is small in comparison to the y_A signal, resulting in the off-diagonal elements of matrix G being nonzero but of a small magnitude compared to the diagonal elements of matrix G.

The same calibration load was applied at each calibration point on the model. In the tunnel the loading distribution will not be well represented by a uniform load at each calibration point. To make up an impulse response for the balance that is representative of the tunnel loading distribution, different scaling factors can be applied to each calibration load. The scaling factors used for the present balance were based on force distributions predicted for a simplified model of the scramjet with no fuel injection.

As a check on the performance of the force balance, the strain signals obtained for each point calibration load can be deconvolved with this global impulse response function. The degree to which the balance recovers each of the calibration loads, in terms of level accuracy and response time, is an indication of how sensitive the balance is to load distribution. The ability of the balance to extract the applied load from the strain signals obtained from a single point load using an impulse response formed from a combination of point loads provides a rigorous test of the balance. In all cases the relative error of the applied load to the deconvolved load was less than 2% (averaged over a 5-ms test window), and the response time (the time for the recovered signal from a step load to reach 90% of the true load) was approximately 0.25 ms.

Despite the good recovery of the mean load levels, it is noted that the noise levels on some of the signals was very high (up to 30% of the applied load) but was of a frequency of the order of a kilohertz and higher. The high noise levels are not unexpected when attempting to recover point loads using a distributed load impulse response function because the timing of stress wave arrivals and reflections at the strain measurement locations will be different for the point load case than would be obtained if the same load had been applied with a different distribution. The deconvolution procedure interprets the different strain signals as being caused by different force time histories rather than being caused by different load distributions.

A test of the sensitivity of using an impulse response determined from 10 point loads for deconvolving signals from shots in the shock tunnel can be made using FEA results. A simulated tunnel-type loading can be composed by applying pressure distributions (and/or multiple point loads) to the FEA model and finding the resulting y_N, y_A, and y_M strain signals. These signals can then be deconvolved using the impulse response obtained from the 10 calibration point loads. This type of test is extremely useful as it simulates a more realistic loading that the scramjet will be subjected to during experimental testing. The loadings for both a fuel-on and fuel-off loading case were tested. The loadings were composed of a simulated pressure loading applied to each surface of the scramjet model and a small number of point loads to simulate the skin-friction component of force. The time histories of the applied loads were chosen to simulate those expected in the experiment. The force rises toward a steady level in 2 ms and then begins to drop off after a further 5 ms.

The applied time histories for axial, normal, and moment loads and the recovered signals for a simulated fuel-off shot are shown in Fig. 4a. These traces were generated by using FEA to predict y_N, y_A, and y_M signals for the force and pressure loading for a simulated fuel-off shot. The signals were then deconvolved using the impulse response obtained from the 10-point calibrations and the forces transformed into lift, thrust, and pitching-moment components. The signals in Fig. 4b were generated using a similar procedure, but the force and pressure loading applied was that for a simulated fuel-on shot. The major difference between the two loading distributions occurs inside the combustion chamber and on the thrust surface where the pressures are increased by a factor of about 15 for the fuel-on case. The increase in pressure leads to a 31% increase in lift, a 2% decrease in thrust, and a 26% decrease in pitching
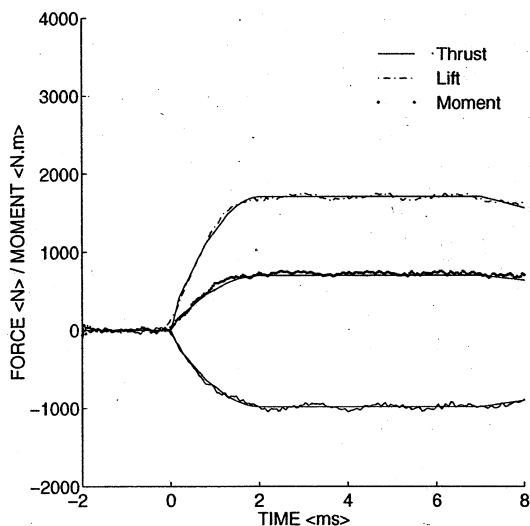
a) Deconvolved fuel-off loading
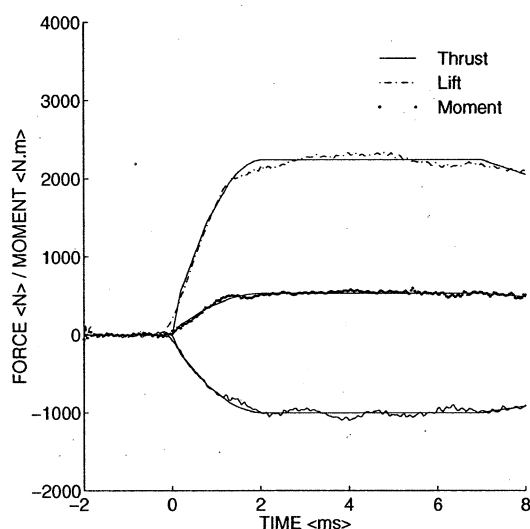
b) Deconvolved fuel-on loading

Fig. 4 Original and deconvolved tunnel-type pressure loadings.

a) Experimental

b) FEA

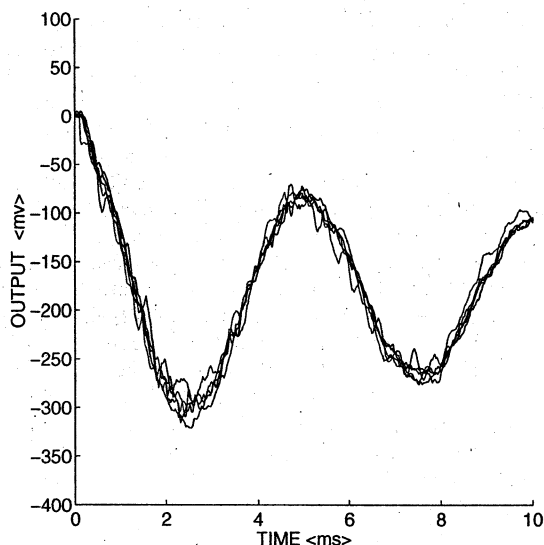Fig. 5 Comparison of axial step responses: experimental and FEA.

moment. The same impulse response function was used to recover the applied loads in the two cases.

The results show that this simulated balance is able to recover both loadings well. The relative errors in thrust, lift, and pitching-moment signals (averaged from 2 to 7 ms) were less than 2% for both the fuel-off and fuel-on loading cases.
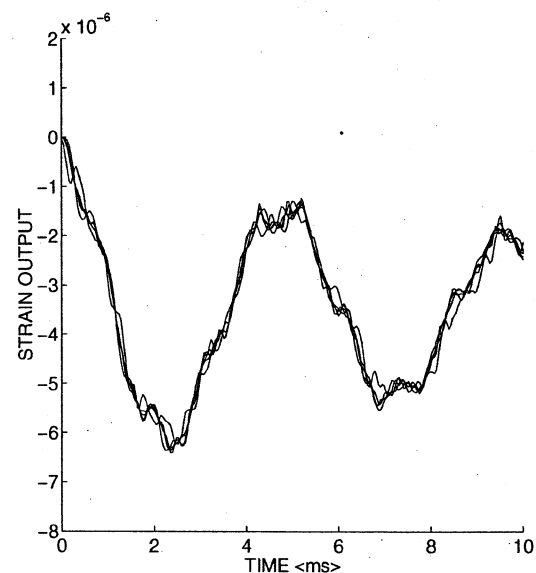
Experimental Calibration of the Balance

Experimental calibration of the force balance was performed by cutting fine wires attached to weights at the calibration points specified in Fig. 1. Cutting the wire produces a step change in the load on the model, and the impulse response can be found by differentiating the step response with respect to time. This calibration technique has been used for both single-[21] and multiple-component[11] stress-wave force balances.

The five axial responses $\epsilon_b(t)$ caused by the five axial point calibration loads as measured by the semiconductor strain gauge are shown in Fig. 5a. (Note that absolute calibrations for the strain gauges were not made so that in this, and subsequent plots, the magnitudes of the measured experimental strain responses are shown directly in terms of the voltage outputs from the strain-gauge amplifiers. Note that the calibration load applied at point A_05 was 87.4% of that applied at the other axial calibration points. The strain signal for A_05 has been inverted and multiplied by 1.14 for comparison in Fig. 5a.) The experimental step calibration responses can be directly compared with the FEA responses shown in Fig. 5b. The

good qualitative agreement between Figs. 5a and 5b illustrates that the FEA is able to model the response of the system including the fundamental frequency of oscillations and damping caused by the rubber pad under the inertial mass. A difference of approximately 5% in the natural frequency of the axial response is noted and is attributed to the estimation of the stiffness for the grounded springs attached to the inertial mass.
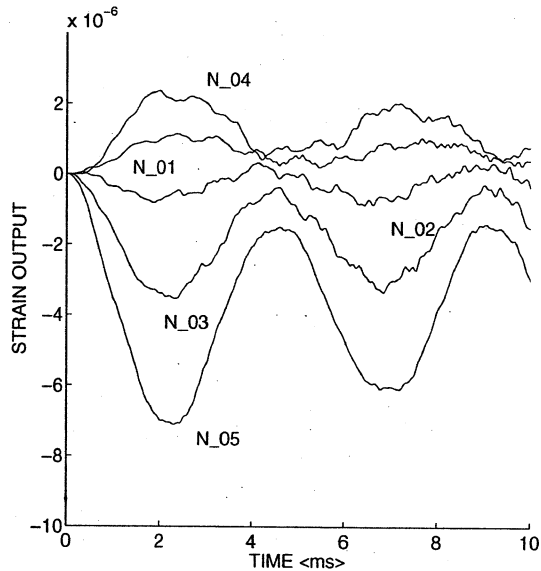
A comparison of the experimental (semiconductor strain-gauge results) with the FEA strain responses in the aft normal stress bar [$\epsilon_a(t)$ signals] for the five normal calibration loads is shown in Figs. 6a and 6b. Some differences are noted. First, the experimental responses are damped. This is attributed to a small amount of free play in the pin joints used at the ends of the normal bars. Because the high-frequency content is present at early times but decays at later times, it is unlikely that the damping is caused by the end condition imposed on the aft normal stress bar as the responses for the axial stress bar, which had no pin joints but a similar end condition, contained high-frequency content over all times. Similar damping has been seen in previous stress-wave force-balance models where the connection between the model and stress bar was poor. Second, a difference of approximately 5% in natural frequency is seen. The difference in frequency is attributed to differences between the FEA and the experiments in the end conditions on the upper supports for the normal bars. A perfectly rigid end condition was applied there
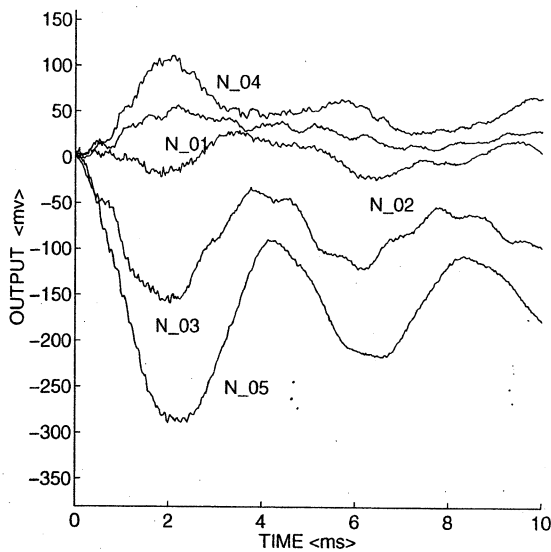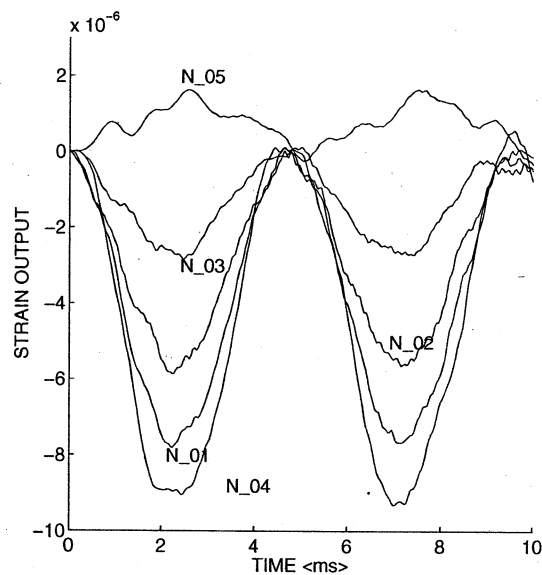
a) Experimental aft bar
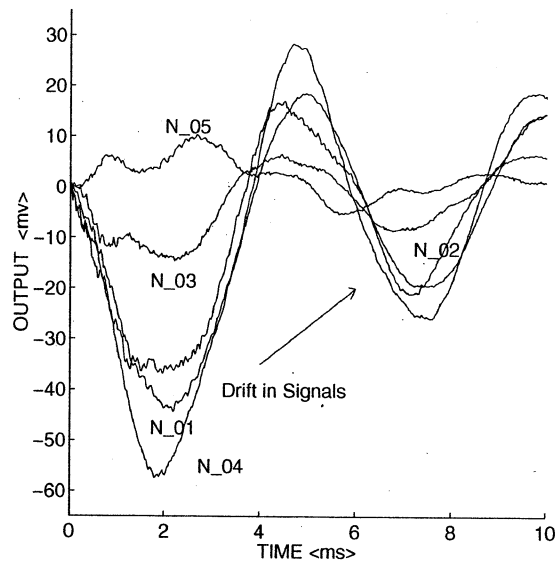
c) Experimental forward bar

b) FEA aft bar

d) FEA forward bar

Fig. 6   Comparison of normal step responses: experimental and FEA.

in the FEA, but in the experiment the upper supports were bolted to the top of the cylindrical dump tank of HYPULSE. This different end condition will result in an overestimation of the stiffness in the FEA model, and hence the frequency of oscillations of the signals in the normal stress bars will be higher than those measured experimentally.

Figures 6c and 6d show comparisons of the strain signals measured in the forward normal bar using the piezoelectric film gauge with the results from the FEA model when the five, normal calibrations loads were applied. Figure 6c clearly shows the drift in the experimental $\epsilon_f(t)$ responses toward the zero level, whereas the FEA responses show no such drift. This is similar to what was seen in the $\epsilon_b(t)$ signals from the piezoelectric film strain gauge. However, because no semiconductor gauge was used on the forward normal bar verification of this drift is not possible, but comparison with the FEA and the aft normal bar strain signals does suggest this.

A global impulse response was formed from the 10-point calibration test results. The strain outputs from each of the calibration point loads were deconvolved with this impulse response to test the performance of the balance, in the same way that the FEA model of the balance was tested. The performance was very similar to that of the FEA model with a similar response time of about 0.25 ms and loads capable of being recovered to within 3% of the applied point

loads when averaged over a 5-ms test window. Thus the physical implementation of the force balance showed a similar performance to that of the FEA simulation in terms of insensitivity to loading distribution and response time.

Prediction of Forces

To check the forces measured in the experiments, some estimates of the pressures and skin friction acting on the surfaces of the model have been made. The fact that the scramjet model is constructed primarily from flat surfaces makes a simple approach to such an analysis appropriate. However, several simplifying assumptions still need to be made for the analysis so that an accurate prediction of the overall forces is not expected.

Because of the presence of side plates on the thrust surface and below the cowl (see Fig. 2), the flows in those regions were approximated as two dimensional. Two-dimensional analysis was also applied to the surfaces within the combustor. Simple oblique shock wave and Prandtl–Meyer relations were used to determine the pressures acting on most of the surfaces, and skin friction was accounted for using laminar and turbulent, flat-plate predictions. The effects of combustion of fuel in the burner were estimated using simple models for the heat released for the fuel used.

To keep the analysis simple, the oblique shock wave from the leading edge of the spatular inlet surface was assumed to hit the lip of the cowl and cancel so that there is no reflected shock transmitted into the combustion chamber and no spillage of the inlet flow occurs. In fact the shock is expected to strike the cowl slightly downstream of its leading edge for the present test conditions (see what follows). It was also assumed that the pressures on the top and bottom surfaces of the combustion chamber were equal, and, because they are parallel and of equal area they produced no net pressure force and no pitching moment. The pressure acting on the thrust surface was determined from the expansion of the flow from the exit of the combustion chamber. Any interactions of waves from the trailing edge of the cowl with the thrust surface were not considered. The significance of these assumptions has been checked using an inviscid computational code for the internal flow path (see what follows). The pressure acting on the sides of the spatular inlet was estimated as the average of the pressure on the top and bottom surfaces of the spatular. The pressure acting on the top surface of the scramjet (where the normal stress bars connect to the scramjet model) was estimated using a pressure coefficient of 0.01 to account for flow spillage from the spatular and from the side walls of the scramjet. The same pressure was applied on the small, nearly vertical surface at the rear of the thrust surface. Forces on the leading and trailing edges of the side plates were neglected. The axial bar protrudes from the thrust surface, and some interference with the flow in that region is expected. The bar is 25 mm wide, and the thrust surface is 100 mm wide. To account for interference, the effective area of the thrust surface was reduced by 25%.

The forces caused by skin friction were calculated using flat-plate, zero-pressure-gradient approximations. On surface regions where the boundary layer was assumed to be laminar, skin frictional forces were calculated using a reference temperature method with Eckert's reference temperature.[22] A simple $Re_\theta/Ma = $ const transition criterion (see, e.g. Ref. 23) was used. An instantaneous transition to turbulence was assumed to occur when Re_θ/Ma exceeded 150, and the momentum thicknesses of the laminar and turbulent boundary layers at that point were set to be equal. The theory of Spalding and Chi[24] was used to calculate the viscous forces caused by turbulent skin friction.

For the fuel-on cases one-dimensional Rayleigh flow was used, and all of the heat release was applied at the start of the combustion chamber. The conditions then remained uniform throughout the combustion chamber until the Prandtl–Meyer relations were used to expand the flow over the thrust surface. The fuel used in the experiments was a mixture of 20% silane (SiH_4) and 80% hydrogen (by volume). The heat released was determined by applying the energy equation with the enthalpies of formation and specific heats along with the mass flow rate of fuel, according to the reactions

$$SiH_4(g) + 2O_2(g) \Rightarrow SiO_2(g) + 2H_2O(g)$$

$$2H_2(g) + O_2(g) \Rightarrow 2H_2O(g)$$
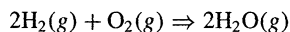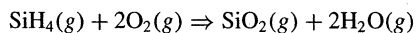
Dissociation of water vapor was not accounted for, and the silicon dioxide was assumed to stay in the vapor phase as a result of the combustor temperature being above the condensation temperature. (The effect of cold walls was neglected.) The final combustor temperature was chosen so that the mean combustor pressure from the modeling matched that measured experimentally, resulting in a combustor efficiency of 63%. This efficiency accounts for incomplete mixing and combustion and other heating losses. This efficiency is of a similar magnitude to that used for CFD predictions on HyperX for a fuel-rich mixture at Mach 7 (Ref. 25).

The forces predicted using this modeling at flow conditions A of Table 1 for fuel-off and fuel-on (at an equivalence ratio Φ of 1.0) are presented in Table 2. For the fuel-off condition the theoretical modeling predicts a lift-to-drag ratio of much less than two at this high angle of attack, reflecting the fact that this design is for combustion investigations rather than for a vehicle capable of producing nett thrust. A positive pitching-moment coefficient indicates a pitching-up moment about the center of the balance. The modeling indicates

Table 1   Nominal Reflected Shock Tunnel test conditions

Test condition	p_∞, kPa	Q_∞, K	ρ_∞, kg/m³	v_∞, m/s	Ma_∞, core
A	1.0	200	0.017	2070	7.3
B	2.0	730	0.010	3300	6.1
C	1.5	200	0.026	2070	7.3

Table 2   Theoretical and computational force estimates for test condition A

Φ	Quantity	Theory	CFD	CFD % error rel. to theory
0.0	Lift, N	1710	1740	2
	Thrust, N	−980	−1000	2
	Moment, N · m	720	740	3
1.0	Lift, N	2240	2410	8
	Thrust, N	−1000	−980	−2
	Moment, N · m	530	510	−4

that burning fuel at $\Phi = 1.0$ at this condition leads to a heat addition of 1.1 MJ/kg of air passing through the burner. As shown in Table 2, this produces a 31% increase in lift, a 2% decrease in thrust, and a 26% decrease in pitching moment. The increase in drag with combustion at an equivalence ratio of 1.0 appears surprising at first. This drag increase comes from increases in the skin frictional forces in the combustion chamber and exhaust surfaces when the fuel burns. This would normally be offset by the pressure increases on the thrust surfaces of the vehicle. However, the thrust surface for the present angle of attack is nearly parallel to the direction of the flow upstream of the scramjet. Thus while the pressure increase on the thrust surface changes the axial force significantly, it actually produces little change in the thrust force on the vehicle.

The suitability of the approximations used in modeling the flow through the combustor was checked using a two-dimensional inviscid computational code.[26] Figure 7a shows contours of $\ell_N p$ for the internal flow for condition A with fuel-off. It can be seen that the shock wave that is initiated from the leading edge of the spatular inlet enters the combustion chamber and reflects back and forth across the chamber. This simulation predicts that the last reflection of this shock off the cowl strikes the thrust surface just before the end of the model. This provides a higher pressure on the rear of the thrust surface and a lower pressure on the forward section of the thrust surface than that predicted using the preceding simple theoretical approach. However, because the pressures acting on the top and bottom surfaces of the combustion chamber are not equal for the CFD result a net normal force is produced in the combustion chamber. It turns out that this decrease in lift in the combustion chamber compensates for the increase in lift at the end of the thrust surface to produce a similar overall lift force to that predicted with the simple model. A similar compensation occurs for moments so that the pitching moments predicted with the two methods agree quite well (Table 2).

The sensitivity of the forces on the model to the way in which heat is released by combustion was also considered. Combustion was simulated in the code by the uniform addition of heat to the source term of the energy equation, beginning 100 mm downstream of the injectors. This location for the start of heat release was based on ignition delay times measured for similar flow conditions in the T3 shock tunnel for the same silane/hydrogen concentration mixtures.[27] Heat was added uniformly until the beginning of the thrust surface. The resulting contours of pressure for the internal flow path for the case of combustion (with a fuel equivalence ratio of 1.0) are shown in Fig. 7b. The heat release reduces the Mach number in the burner and changes the trajectory of the shock from the leading edge of the inlet as it passes down the combustion chamber. Table 2 summarizes the resulting comparison between the theoretical estimates just described and those with the inviscid internal flowfield forces replaced with the CFD results. The forces and moments on the model generated when the internal flow path is calculated using the CFD code
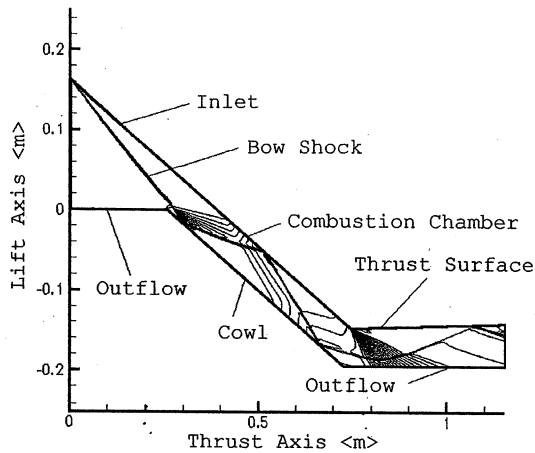
a) $\Phi = 0.0$
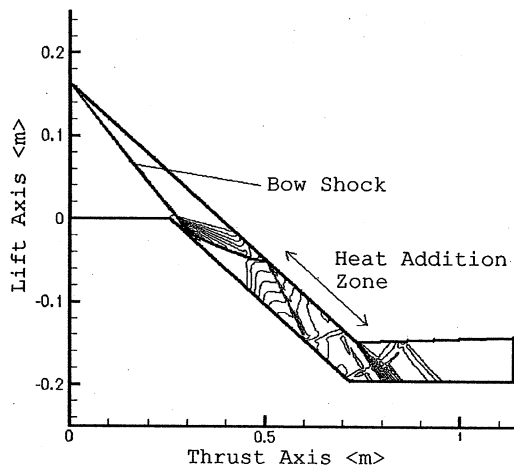
b) $\Phi = 1.0$

Fig. 7 Contours of $\ell_n p$ for the internal flowfield for condition A.

a) $\Phi = 0.0$

b) $\Phi = 1.0$.

Fig. 8 Deconvolved lift, thrust, and pitching-moment time histories for condition A.

are similar to those for the simple model. The largest difference occurs in the lift with combustion (a difference of 8%). Additional simulations were run using shorter residence times before heat release. These resulted in differences in the predicted forces of up to 10%.

Experimental Results

Experimental testing of the force balance and scramjet was carried out at Mach 7 and Mach 10 enthalpies (see Table 1) in the HYPULSE facility. The Mach 7 enthalpy tests were obtained by using a helium-gas driver at ambient temperature, whereas the Mach 10 enthalpy condition used a shock-induced detonation driver section. HYPULSE was configured in reflected shock-tunnel mode with establishment of steady flow within 1 ms of the shock arrival at the nozzle exit and contamination by the driver occurring after approximately 7 ms for the Mach 7 enthalpy condition. Contamination caused by water vapor for the Mach 10 enthalpy condition is estimated to be at 4 ms after shock arrival.

In Fig. 8a the deconvolved lift, thrust, and pitching-moment coefficient time histories are compared with theoretical force coefficients for fuel-off tests at condition A. The deconvolved time histories of force were filtered with first-order Butterworth filter with a cutoff frequency of 5 kHz. The reference area used in the coefficients is the capture area of the intake of the scramjet. For the present model this was 0.0166 m². The dynamic pressure used in determining the force coefficients has been related to the measured pressure in the nozzle supply region so that any variations in supply conditions can be accounted for. For high Mach numbers ($Ma^2 \gg 1$) and a gas with a ratio of specific heats of 1.4, the Rayleigh–pitot formula can be used to show that
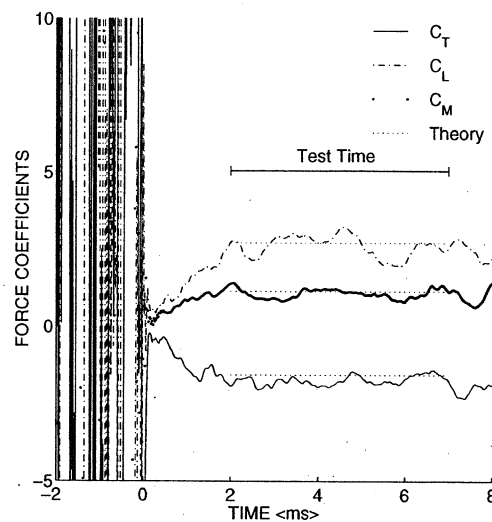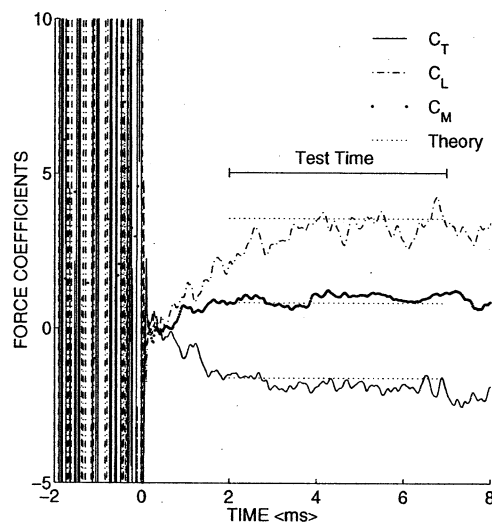
$$p_P \approx 0.92 \rho_\infty v_\infty^2 \tag{5}$$

Pitot pressure was not measured directly in the present tests, but nozzle calibration studies for HYPULSE show that the ratio of pitot to nozzle supply pressure is 0.0095 for the present condition.[25] If p_s is the measured nozzle supply pressure, the dynamic pressure $\frac{1}{2}\rho_\infty v_\infty^2$ can be written as

$$\tfrac{1}{2}\rho_\infty v_\infty^2 = 5.16 \times 10^{-3} p_s \tag{6}$$

Equation (6) was used with the measured nozzle supply pressure time history to determine the force coefficients.

The time histories of the force coefficients in Fig. 8a are clearly less steady than the deconvolved time histories for forces in the simulations already discussed (see Fig. 4a). The oscillations in the deconvolved signals were larger for the Mach 10 enthalpy condition that also had a shorter duration test flow. Separate accelerometer tests, measuring the vibration of the test section, showed a similar frequency of oscillation to that seen in the deconvolved signals. This suggests that the present results are affected by the vibration of the test section because of tunnel operation. Any vibrations that induce strains in the stress bars will be interpreted by the deconvolution calculations as fluctuating forces on the model. The results indicate that the oscillations are larger on the deconvolved lift signal than on the drag signal, suggesting that the normal bars, which were directly connected to the top of the test section and contribute more to the lift signal, were affected more than was the axial bar. Subsequent experiments on three-component force measurement using stress-wave force balances have indicated the importance of

Table 3 Comparison of experimental and theoretical force coefficients for test condition A

Φ	Quantity	Theory	Exp.	Exp. % error rel. to theory
0.0	C_L	2.72	2.61	−4
	C_T	−1.56	−1.72	−10
	C_M	1.14	1.07	−6
	C.P.[a] (% of chord)	28	26	−2
1.0	C_L	3.56	3.16	−11
	C_T	−1.59	−1.81	−14
	C_M	0.84	0.99	18
	C.P. (% of chord)	16	20	4

[a]C.P. = axial center of pressure.

a) $\Phi = 0.0$

b) $\Phi = 0.0$

Fig. 9 Deconvolved lift, thrust, pitching-moment, and center-of-pressure time histories for condition C scaled by the operating pressure to condition A and compared with deconvolved lift, thrust, pitching-moment, and center-of-pressure time histories for condition A.

employing some vibration isolation of the balance to reduce noise in the signals.[28] Despite the noise on the signals, the results at the Mach 7 enthalpy condition, with its longer test time, still enable analysis of the results.

The measured force coefficients for the fuel-off test at condition A are compared with the predictions of the analysis in the plot in Fig. 8a. The measured lift coefficient is within 4% of the predicted value, but the thrust coefficient is underpredicted by 10% (i.e., the measured drag is higher than that predicted). The center of pressure is predicted to within 2% of the chord of the measured value. The center of pressure is presented in terms of the distance in the axial direction from the center of mass to the line of action of the aerodynamic force on the model. This distance is given as a percentage of the axial chord length of the model (1.165 m), and a positive value indicates a line of action upstream of the center of mass. The center of mass of the scramjet vehicle was located 615 mm from the leading edge of the spatular in the axial direction and −33 mm from the leading edge in the normal direction. Given the levels of approximation in the theoretical analysis, the agreement between the experiments and theory is considered good.

The time histories of the force coefficients when the fuel is turned on at an equivalence ratio of 1.0 are shown in Fig. 8b. There is little change in the noise level on the signals. It can be seen that the lift and pitching-moment coefficients change when the fuel burns, but there is little change in the thrust coefficient. These trends agree with the theoretical calculations. The theoretical coefficients are also shown in Fig. 8b, and the mean levels during the test time are compared in Table 3. The lift coefficient is predicted to increase more than was measured, but the measured and predicted levels still agree to within 11%. A larger increase in drag was measured than was predicted and such that the predicted thrust coefficient is 14% higher than that measured. As already discussed, the increase in drag with fuel on is attributed to increases in skin-frictional forces in the combustion chamber and the fact that the thrust surface is nearly parallel to the oncoming flow direction for the present angle of attack of the model. The higher pressures on the thrust surface lead to a decrease in pitching-up moment on the model with combustion. The change in the center of pressure is less than predicted, but the measured center of pressure with burning is within 4% of the model chord of that predicted.

A fuel-off test was also done at a condition with a higher nozzle-supply pressure, condition C, as a check on the linearity of the force balance. The enthalpy and flow speed at condition C are similar to those at condition A, but the pressure and density levels are 50% higher (see Table 1). The force coefficients measured at condition C have been scaled by a factor of $\frac{2}{3}$ to compare with those measured for condition A. Results are shown in Fig. 9a. Also shown for reference are the time histories of the line of action of the resulting force shown as a percentage of chord in Fig. 9b. It can be seen that the results scale well. The mean lift and thrust coefficients during the test period agree to within 10 and 13%, respectively. The centers of pressure agree to within 3% based on the chord length. Thus the balance is seen to be linear over the range of forces tested.

The calibration and bench tests of the force balance indicate that it is capable of measuring lift and thrust forces to an accuracy of 3% and the line of action of the resultant force to within 3% of
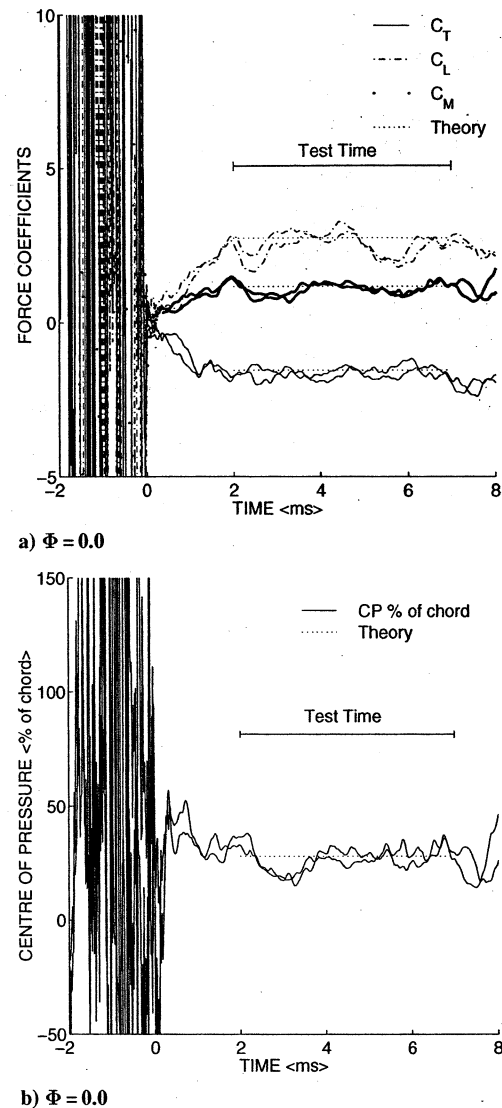
the chord of the model. These levels are in line with the results of the finite element simulations. However, the influence of vibration entering the balance through its supports caused a deterioration of the performance of the balance during the tunnel tests. Based on comparisons with theoretical calculations of the force levels, it is estimated that the accuracy of the measurements in the tunnel tests was around 15% for force measurements and 5% of chord for line of action of the force. It is expected that these errors could be reduced with better vibration isolation techniques applied to the balance mounting arrangements.

Conclusions

Because of the short test times in shock-tunnel facilities, conventional force measurement techniques cannot be used. A method recently developed, the stress-wave force-balance technique, allows measurement of forces in test times of the order of milliseconds. This technique has been used to measure the three components of force on a fueled scramjet model. Of significance is the large size and mass of the model. The model weighs in excess of 40 kg and is over 1.165 m long.

Finite element modeling of the force-balance design was performed and gave valuable insight into the broad trends and capabilities of the balance. By applying a series of point calibration loads, as can readily be done on a physical balance, an impulse

response function for the balance was assembled. Deconvolution of the balance strain outputs was used to determine the ability of the balance to measure force time histories for varying types of loading distributions. Of particular interest is the sensitivity to a change in loading distribution, with an associated shift in the center of pressure, and the ability of the balance to resolve the associated lift and thrust forces. Such a capability is important for tests on airframe-integrated scramjet engines. Simulations showed that the present arrangement is suitable for such measurements.

Calibration tests on the force balance showed that the finite element analysis was capable of predicting strain time histories for step loads, and the overall performance of the simulated balance was similar to that measured. Experimental bench testing of the force balance indicated that the point calibration loads could be recovered to within 3% of the applied point load when averaged over a 5-ms test window. By minimizing force transmission from the tunnel to the balance and careful aerodynamic shielding of the balance structure, measurement errors of a similar magnitude for tests in a shock tunnel should be achievable.

Tests of the scramjet and force balance in the HYPULSE shock tunnel indicated that the balance was influenced by vibrations of the test section that were induced by the operation of the tunnel. Better vibration isolation of the balance is recommended. Nevertheless, force measurements with and without combustion were made at a Mach 7 condition, and measurements agreed reasonably with approximate theoretical predictions of the performance of the scramjet. Tests at a higher pressure level, also at the Mach 7 condition, demonstrated linearity of the force balance.

Acknowledgments

References

[1]McClinton, C. R., Rausch, D. R., Sitz, J., and Reukauf, P., "Hyper-X Program Status," AIAA Paper 2001-1910, April 2001.

[2]Bernstein, L., "Force Measurement in Short-Duration Hypersonic Facilities," AGARDograph 214, Nov. 1975.

[3]Campbell, B. T., Siwbenhaar, A., and Nguyen, T., "Strutjet Engine Performance," Journal of Propulsion and Power, Vol. 17, No. 6, 2001, pp. 1227–1232.

[4]Cockrell, C. E., Engelund, W. C., Bittner, R. D., Jentink, T. N., Dilley, A. D., and Frendi, A., "Integrated Aeropropulsive Computational Fluid Dynamics Methodology for the Hyper-X Flight Experiment," Journal of Spacecraft and Rockets, Vol. 38, No. 6, 2001, pp. 836–843.

[5]Mitani, T., Hiraiwa, T., Sato, S., Tomioka, S., Kanda, T., and Tani, K., "Comparison of Scramjet Engine Performance in Mach 6 Vitiated and Storage-Heated Air," Journal of Propulsion and Power, Vol. 13, No. 5, 1997, pp. 635–642.

[6]Gruber, M., Donbar, J., Jackson, K., Mathur, T., Baurle, R., Eklund, D., and Smith, C., "Newly Developed Direct-Connect High-Enthalpy Supersonic Combustion Research Facility," Journal of Propulsion and Power, Vol. 17, No. 6, 2001, pp. 1296–1304.

[7]Carbonaro, M., "Aerodynamic Force Measurements in the VKI Long Shot Hypersonic Facility," New Trends in Instrumentation for Hypersonic Research, edited by A. Boutier, Kluwer Academic, Norwell, MA, 1992, pp. 317–325.

[8]Störkmann, V., Olivier, H., and Grönig, H., "Force Measurements in Hypersonic Impulse Facilities," AIAA Journal, Vol. 36, No. 3, 1998, pp. 342–348.

[9]Naumann, K. W., Ende, H., Mathieu, G., and George, A., "Millisecond Aerodynamic Force Measurement with Side Jet Model in the ISL Shock Tunnel," AIAA Journal, Vol. 31, No. 6, 1993, pp. 1068–1074.

[10]Sanderson, S. R., and Simmons, J. M., "Drag Balance for Hypervelocity Impulse Facilities," AIAA Journal, Vol. 29, No. 12, 1991, pp. 2185–2191.

[11]Mee, D. J., Daniel, W. J. T., and Simmons, J. M., "Three-Component Force Balance for Flows of Millisecond Duration," AIAA Journal, Vol. 34, No. 3, 1996, pp. 590–595.

[12]Paull, A., Stalker, R. J., and Mee, D. J., "Scramjet Thrust Measurement in a Shock Tunnel," Aeronautical Journal, Vol. 99, No. 984, 1995, pp. 161–163.

[13]Stalker, R. J., and Paull, A., "Experiments on Cruise Propulsion with a Hydrogen Scramjet," Aeronautical Journal, Vol. 102, No. 1011, 1998, pp. 37–43.

[14]Takahashi, M., Ueda, S., Komuro, T., Sato, K., Tanno, H., and Itoh, K., "Development of a New Force Measurement Method for Scramjet Testing in a High Enthalpy Shock Tunnel," AIAA Paper 99-4961, Nov. 1999.

[15]Prost, R., and Goutte, R., "Discrete Constrained Iterative Deconvolution Algorithms with Optimized Rate of Convergence," Signal Process, Vol. 7, No. 3, 1984, pp. 209–230.

[16]Orth, R. C., Kislykh, V. V., and Erdos, J. I., "Data Analysis from Hypersonic Combustion Tests in the TSNIIMASH PGU-11 Facility," AIAA Paper 96-4584, Nov. 1996.

[17]Smith, A. L., Mee, D. J., Daniel, W. J. T., and Shimoda, T., "Design, Modelling and Analysis of a Six-Component Force Balance for Hypervelocity Wind Tunnel Testing," Computers and Structures, Vol. 79, No. 11, 2001, pp. 1077–1088.

[18]Smith, A. L., and Mee, D. J., "Dynamic Strain Measurement Using Piezoelectric Polymer Film," Journal of Strain Analysis for Engineering Design, Vol. 31, No. 6, 1996, pp. 463–465.

[19]Daniel, W. J., and Mee, D. J., "Finite Element Modelling of a Three-Component Force Balance for Hypersonic Flows," Computers and Structures, Vol. 54, No. 1, 1995, pp. 35–48.

[20]Blakely, K., Basic Dynamic Analysis, User Guide, McNeal–Schwendler Corp., Los Angeles, 1993.

[21]Tuttle, S. L., Mee, D. J., and Simmons, J. M., "Drag Measurements at Mach 5 Using a Stress Wave Force Balance," Experiments in Fluids, Vol. 19, No. 5, 1995, pp. 336–341.

[22]White, F. M., Viscous Fluid Flow, 2nd ed., McGraw–Hill, New York, 1991, pp. 511, 512.

[23]Bertin, J. J., Stetson, K. F., Bouslog, S. A., and Caram, J. M., "Effect of Isolated Roughness Elements on Boundary-Layer Transition for Shuttle Orbiter," Journal of Spacecraft and Rockets, Vol. 34, No. 4, 1997, pp. 426–436.

[24]Spalding, D. B., and Chi, S. W., "The Drag of a Compressible Turbulent Boundary Layer on a Smooth Flat Plate with and Without Heat Transfer," Journal of Fluid Mechanics, Vol. 18, Jan. 1964, pp. 117–143.

[25]Rogers, R. C., Shih, A. T., Tsai, C. Y., and Foelsche, R. O., "Scramjet Tests in a Shock Tunnel at Flight Mach 7, 10 and 15 Conditions," AIAA Paper 01-3241, July 2001.

[26]Craddock, C., and Jacobs, P., "A Space Marching Compressible Flow Solver with Chemistry and Optimization," Dept. of Mechanical Engineering, Univ. of Queensland, TR 6/98, Australia, June 1998.

[27]Morris, N. A., "Silane as an Ignition in Scramjets," M.S. Thesis, Dept. of Mechanical Engineering, Univ. of Queensland, Brisbane, Australia, Dec. 1989.

[28]Robinson, M. J., Mee, D. J., and Paull, A., "Lift, Pitching Moment and Thrust Measurement on a Fuelled Scramjet," Proceedings of the Twenty-Third International Symposium on Shock Waves, edited by F. K. Lu, Univ. of Texas, Arlington, TX, 2002, pp. 500–507.

M. S. Miller
Associate Editor